Nano Research 2017, 10(12): 4436–4447
DOI 10.1007/s12274-016-1343-z
Research Article
ISSN 1998-0124
CN 11-5974/O4

Iron-chelated hydrogel-derived bifunctional oxygen electrocatalyst for high-performance rechargeable Zn–air batteries

Fanlu Meng[1,2], Haixia Zhong[1,3], Junmin Yan[2] (✉), and Xinbo Zhang[1] (✉)

[1] *State Key Laboratory of Rare Earth Resource Utilization, Changchun Institute of Applied Chemistry, Chinese Academy of Sciences, Changchun 130022, China*
[2] *Key Laboratory of Automobile Materials, Ministry of Education and College of Materials Science and Engineering, Jilin University, Changchun 130012, China*
[3] *University of Chinese Academy of Sciences, Beijing 100049, China*

Received: 24 August 2016
Revised: 14 October 2016
Accepted: 19 October 2016

KEYWORDS
hydrogel,
iron-nitrogen-doped carbon,
bifunctional,
oxygen reduction reaction (ORR),
oxygen evolution reaction (OER),
Zn–air batteries

ABSTRACT

Efficient oxygen electrocatalysts are the key elements of numerous energy storage and conversion devices, including fuel cells and metal–air batteries. In order to realize their practical applications, highly efficient and inexpensive non-noble metal-based oxygen electrocatalysts are urgently required. Herein, we report a novel iron-chelated urea-formaldehyde resin hydrogel for the synthesis of Fe-N-C electrocatalysts. This novel hydrogel is prepared using a new instantaneous (20 s) one-step scalable strategy, which theoretically ensures the atomic-level dispersion of Fe ions in the urea-formaldehyde resin, guaranteeing the microstructural homogeneity of the electrocatalyst. Consequently, the prepared electrocatalyst exhibits higher catalytic activity and durability in the oxygen reduction (ORR) and evolution (OER) reactions than the commercial Pt/C catalyst. Furthermore, the above catalyst also shows a much better performance in rechargeable Zn–air batteries, including higher power density and better cycling stability. The developed synthetic approach opens up new avenues toward the development of sustainable active electrocatalysts for electrochemical energy devices.

1 Introduction

The ever-growing energy demand necessitates the urgent development of new energy conversion and storage systems that are highly efficient, low-cost, and environmentally friendly [1–3]. Electrochemical technologies such as fuel cells and metal–air batteries can provide a means for the efficient interconversion of chemical and electrical energy [4–6]. The oxygen reduction (ORR) and evolution (OER) reactions are the

Address correspondence to Xinbo Zhang, xbzhang@ciac.ac.cn; Junmin Yan, junminyan@jlu.edu.cn

two most important processes in these electrochemical applications [7–10]; however, their sluggish kinetics cause severe energy efficiency losses. Platinum and its alloys are currently the best ORR catalysts known; however, their industrial application is limited by their high cost and poor stability [11–13]; moreover, they are poor OER electrocatalysts. On the contrary, Ru and Ir oxides exhibit extraordinary OER activity, but show poor ORR performance [14–16]. Consequently, highly active and stable non-precious metal bifunctional electrocatalysts with low cost are urgently required for both the ORR and OER.

Recently, a wide range of alternative non-precious metal-based electroactive materials including carbons [17, 18], metal oxides [19, 20], sulfides [21], and their composites [22] have been developed for both the ORR and OER. Among them, carbons (in particular, N-doped carbons) including graphene [23], carbon nanotubes (CNTs) [24], and porous carbons [25] have demonstrated promising catalytic activity and stability as possible replacements of Pt catalysts. N-doped porous carbons exhibit even more advantages due to their high specific surface area, high flux mass transportation, and efficient utilization of active catalytic sites [26–29]. In particular, doping of these carbons by transition metals produces promising non-precious metal ORR catalysts [30–33] that also show competitive OER catalytic performance [34].

The urea-formaldehyde resin (UFR), containing both carbon and a large amount of nitrogen (38 wt.%), is intrinsically suitable for constructing multifunctional porous N-doped carbons for emerging energy-related applications such as supercapacitors [35] and carbon dioxide absorption [36]. On the other hand, the multiple donor sites (amino and carbonyl groups) in UFR provide an excellent environment for the coordination of transition metal ions, which is undoubtedly beneficial to M-N-C electrocatalysts. However, the traditional multistep synthesis of UFR is usually time-consuming, requiring an additional pore-forming reagent (metal carbonates or silica) to produce porous carbons. In particular, when it comes to the introduction of transition metal ions, the poor compatibility between UFR and transition metal salts (just like in other N-containing polymer/metal salt systems) results in the agglomeration of metal particles and microstructural inhomogeneity of the obtained M-N-C non-precious metal catalysts [37–39]. Therefore, developing a facile effective strategy to realize homogeneous dispersion of transition metal ions in UFR, ideally at an atomic level, is urgently required, but remains a great challenge.

Herein, as a proof-of-concept experiment, we first develop and demonstrate a very fast one-step scalable synthesis of an iron-chelated UFR (Fe-UFR) hydrogel to theoretically ensure the atomic-level dispersion of iron in UFR for constructing a homogeneous metal-/N-containing polymer composite. When the Fe-UFR hydrogel is employed as an all-in-one precursor of the iron-nitrogen-doped porous carbon materials (C-Fe-UFR), these catalysts display higher activity and durability toward ORR and OER, as compared to the commercial Pt/C catalyst in alkaline media. Moreover, the C-Fe-UFR catalysts also exhibit a competitive electrocatalytic ORR performance in acidic media. The corresponding Zn–air batteries show much better electrochemical performances compared to commercial Pt/C systems, e.g., higher power densities. Furthermore, rechargeable Zn–air battery tests indicate their high cycling efficiency, evidenced by a narrow discharge–charge voltage gap and a stable voltage plateau during charging–discharging for up to 100 cycles at a current density of 10 $mA \cdot cm^{-2}$ (20 min per cycle). To our knowledge, the sustainable development of high-performance Fe-N-C catalysts with controlled structure and components based on the economical Fe-UFR hydrogel has never been reported.

2 Experimental

2.1 Synthesis of Fe-UFR hydrogels and C-Fe-UFR catalysts

In a typical procedure, $Fe(NO_3)_3 \cdot 9H_2O$ (1.21 g) was dissolved in a solution of formaldehyde (3.6 mL, 37%) under stirring, followed by the addition of urea (1.8 g) with strong agitation. The Fe-UFR gel obtained after about 20 s was heated to 80 ℃ and kept at this temperature for 12 h, followed by heating in an autoclave at 130 ℃ for another 12 h for further drying. The prepared Fe-UFR was loaded into a tube furnace and heated under N_2 atmosphere at a rate of 3 $℃ \cdot min^{-1}$ to 300 ℃ for 1 h, followed by heating at a rate of

5 ℃·min^{-1} to 900 ℃ for 1 h. The sample was subsequently cooled to room temperature, etched with 3 M HCl under ultrasonication for 8 h, and washed several times with deionized water. Finally, the sample was dried at 80 ℃ for 12 h to yield C-Fe-UFR. For comparison, samples with different iron contents were prepared under the same conditions (sample Fe0.81-UFR for C-Fe0.81-UFR and Fe1.61-UFR for C-Fe1.61-UFR).

2.2 Synthesis of UFR and C-UFR

Urea (1.8 g) was dissolved in a solution of formaldehyde (3.6 mL, 37%) at 45 ℃ under stirring. After about 30 min, hydrochloric acid (20 μL) was added to the above urea/formaldehyde solution under stirring, producing an aqueous UFR solution after about 1 min. The obtained UFR solution was heated to 80 ℃ and kept at this temperature for 12 h, followed by heating to 130 ℃ for another 12 h in an autoclave for further drying to produce UFR. The obtained UFR was mixed with SiO_2 (1.0 g, 5–15 nm) powder using an agate mortar. The obtained mixture was thermally treated, similar to the case of Fe-UFR. Subsequently, the mixture was etched with 20% hydrofluoric acid and washed several times with deionized water. Finally, drying at 80 ℃ for 12 h yielded the C-UFR product.

2.3 Synthesis of UFR/Fe and C-UFR/Fe

Urea (1.8 g) was dissolved in a solution of formaldehyde (3.6 mL, 37%) at 45 ℃ under stirring, and $Fe(NO_3)_3·9H_2O$ (1.21 g) was dissolved in deionized water (1.8 mL). After about 30 min, the above $Fe(NO_3)_3$ solution was poured into the urea/formaldehyde solution under vigorous stirring. About 1 min later, the aqueous UFR/Fe sample was obtained. All experimental procedures for the synthesis of C-UFR/Fe were similar to those used for the preparation of C-Fe-UFR.

2.4 Physical characterization

FTIR spectra were recorded on a Nicolet 6700 spectrometer. Scanning electron microscopy (SEM) analysis was performed using a field emission scanning electron microanalyzer (Hitachi S4800) operated at an accelerating voltage of 10 kV. Transmission electron microscopy (TEM) and elemental mapping were performed on an FEI Tecnai G2 S-Twin instrument with a field emission gun operating at 200 kV. Powder X-ray diffraction (XRD) measurements were carried out using a Bruker D8 Focus powder X-ray diffractometer with Cu Kα (λ = 0.15405 nm) radiation (40 kV, 40 mA). Nitrogen adsorption–desorption measurements were performed on a Micromeritics ASAP 2020 adsorption analyzer. Pore volumes and sizes were estimated based on the pore size distribution curves obtained from the desorption isotherms using the Barrett–Joyner–Halenda (BJH) method, and the specific surface areas were calculated by the Brunauer–Emmett–Teller (BET) method. X-ray photoelectron spectroscopy (XPS) analyses were conducted on a VG Scientific ESCALAB MKII X-ray photoelectron spectrometer using an Al Kα source. All electrochemical measurements were performed on a BioLogic VMP3 electrochemical workstation. The rotating disk electrode (RDE) and rotating ring disk electrode (RRDE) experiments were performed using an MSR electrode rotator (Pine Instrument Co.).

2.5 Electrochemical activity characterization

The RDE and RRDE measurements used to evaluate the catalysts were performed in a conventional three-electrode cell with 0.1 M KOH and 0.1 M $HClO_4$ solutions as electrolytes at room temperature. An RDE of 5.0 mm diameter and an RRDE of 5.61 mm diameter were used as the working electrodes. A platinum foil and Ag/AgCl in saturated KCl were used as the counter and reference electrodes, respectively. All potentials in this study were measured relative to the Ag/AgCl electrode and were subsequently converted to potentials vs. the reversible hydrogen electrode (RHE) according to E(vs. RHE) = E(vs. Ag/AgCl) + 0.197 + 0.059pH. The catalyst ink was prepared by blending the catalyst (5 mg) and 5 wt.% Nafion solution in ethyl alcohol (50 μL) in 1 mL of ethanol under sonication for 30 min. In the case of the alkaline electrolyte, 10 μL of the catalyst ink was applied to the surface of the glassy carbon (GC) disk electrode, yielding a catalyst loading of 0.25 mg·cm^{-2}. For comparison, the Pt/C catalyst ink was prepared by ultrasonically blending 5 mg of Pt/C (a commercially available Pt/C catalyst, nominally 20 wt.% on carbon black from Johnson

Matthey) and 50 μL of a 5 wt.% Nafion solution in alcohol in 1 mL of ethanol for 30 min to obtain a well-dispersed ink. A 10-μL aliquot of the catalyst ink was then drop-cast onto the GC surface, producing a Pt loading of 0.05 mg·cm^{-2}. Cyclic voltammetry measurements were carried out in a N_2- or O_2-saturated electrolyte from –1.0 to 0.2 V vs. Ag/AgCl at a scan rate of 50 mV·s^{-1}. RDE measurements were performed at different rotation speeds in O_2-saturated electrolyte from –1 to 0.2 V vs. Ag/AgCl at a sweep rate of 10 mV·s^{-1}. In the case of the acidic electrolyte, 20 μL of the catalyst ink was applied to the surface of the GC disk electrode, yielding a catalyst loading of 0.50 mg·cm^{-2}, and the potential range was set from –0.2 to ~1 V. For RRDE measurements, the ring potential was set at 0.5 V in 0.10 M KOH and at 1.0 V in 0.1 M $HClO_4$.

The number of electrons transferred to the C-Fe-UFR catalyst was calculated according to the Koutecky–Levich equation

$$1/j = 1/j_d + 1/j_k = 1/(B\omega^{1/2}) + 1/j_k \quad (1)$$

$$B = 0.62nFC_O D_O^{2/3} \nu^{-1/6} \quad (2)$$

where j (mA·cm^{-2}) is the measured current density related to the diffusion-limiting current (j_d) and the kinetic current (j_k), F is the Faraday constant (96,485 C·mol^{-1}), D_O is the diffusion coefficient of oxygen in 0.1 mol·L^{-1} KOH (1.9 × 10^{-5} cm^2·s^{-1}), ν is the kinematic viscosity of water (0.01 cm^2·s^{-1}), C_O is the bulk concentration of oxygen in oxygen-saturated 0.1 mol·L^{-1} KOH (1.2 × 10^{-6} mol·cm^{-3}), ω is the RDE rotation speed, and n is the electron transfer number for the ORR. A linear plot of j_{lim}^{-1} vs. $\omega^{-1/2}$ has a slope of $1/(0.62nFC_O D_O^{2/3}\nu^{-1/6})$, with ω being the angular rotation speed (rad·s^{-1}).

The following equations were used to calculate n (the apparent number of electrons transferred during ORR) and $\%HO_2^-$ (the percentage of HO_2^- released during ORR)

$$n = 4I_D/(I_D + (I_R/N)) \quad (3)$$

$$\%HO_2^- = 200(I_R/N)/(I_D + (I_R/N)) \quad (4)$$

Here, I_D and I_R are the disk and ring currents, respectively, and N = 0.37 is the ring collection efficiency. Linear sweep voltammograms for the OER were obtained using RDE measurements (1,600 rpm) corrected by iR-compensation in 1.0 M KOH at a scan rate of 10 mV·s^{-1} and a catalyst loading of 0.51 mg·cm^{-2}. The solution resistance was determined by the high-frequency intercept of the Nyquist plot obtained by electrochemical impedance spectroscopy (EIS).

2.6 Zn–air batteries

Zn–air batteries were tested as in-house-built electrochemical cells, with the catalyst-loaded carbon fiber paper (1.0 cm^2, 1.0 mg catalyst loading) acting as the air cathode, and a Zn plate acting as the anode. A solution containing 6.0 M KOH and 0.2 M zinc acetate was used as an electrolyte to ensure reversible Zn electrochemical reactions at the anode. The as-fabricated cells were characterized at room temperature using a BioLogic VMP3 electrochemical workstation and a LAND CT2001A multi-channel battery testing system.

3 Results and discussion

The overall synthetic strategy used to prepare C-Fe-UFR is illustrated in Fig. 1. First, ferric nitrate was dissolved in aqueous formaldehyde, forming a homogenous solution and leading to a strongly acidic environment. Second, a certain amount of urea was poured into the above solution under strong agitation, and an implosion was observed. Notably, despite being very rapid (~20 s), this novel and effective synthetic method holds the additional advantage of easy scalability, even for large-scale applications (Fig. S1 in the Electronic Supplementary Material (ESM)). For comparison, a physical mixture of UFR and ferric nitrate (UFR/Fe) was also synthesized (Fig. S2 in the ESM). The formation mechanism of Fe-UFR was primarily investigated by Fourier transform infrared (FTIR) spectroscopy. Figure S3 in the ESM shows that the FTIR spectra of UFR/Fe are almost identical to that of pristine UFR. However, a hump around 3,310 cm^{-1} appears in the spectra of Fe-UFR, in contrast to those of UFR and UFR/Fe; in addition, the width of the hump increases with the amount of added ferric nitrate, which might be attributed to the variational merger of –NH, which is greatly influenced by the metal coordination [40, 41]. The results of XPS analysis provide further evidence for the coordination of

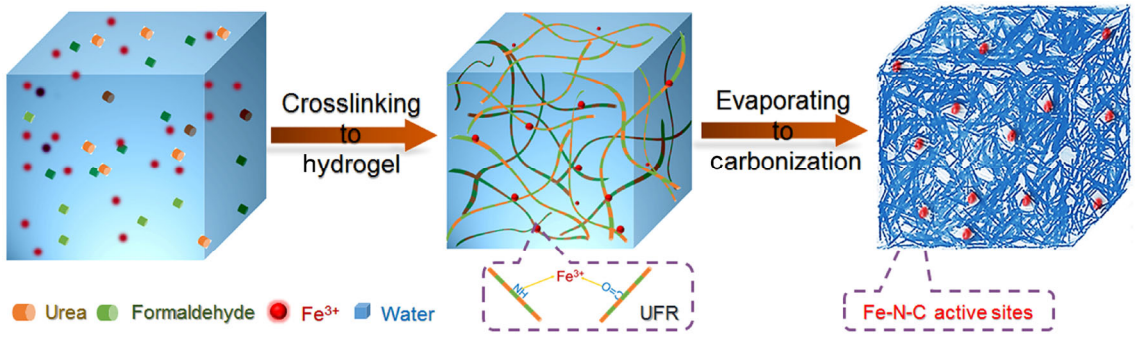

Figure 1 Schematic synthesis of the Fe-UFR hydrogel and the related Fe-N-C electrocatalysts (C-Fe-UFR).

metal centers, whereas the N 1s XPS spectra display positively shifted binding energies compared to that of pristine UFR (Fig. S4 in the ESM). Powder XRD patterns reveal a significant structure change of Fe-UFR compared to pristine UFR, with an amorphous state displacing the peaks of crystalline UFR (Fig. S5 in the ESM) [42]. The completely destroyed crystal structure indicates the existence of physical cross-linkages (coordination between Fe ions and multiple donor sites, e.g., amino and carbonyl groups) between different chains, supported by the good flexibility of Fe-UFR compared to that of UFR and UFR/Fe in the twisting test (Fig. S6 in the ESM). To this end, high-temperature carbonization and acid etching treatments were subsequently carried out to convert the homogeneous composite hydrogel (Fe-UFR) into porous Fe-N-C materials (C-Fe-UFR).

The typical SEM image in Fig. 2(a) confirms the porous structure of C-Fe-UFR, and TEM imaging (Fig. 2(b)) further reveals its microstructure with abundant and homogenously distributed pores. In contrast, C-UFR/Fe seems to have an agglomerated morphology and a less porous structure (Fig. S7 in the ESM). The surface area and porosity of C-Fe-UFR were further investigated by nitrogen adsorption–desorption. Typical type-IV isotherms indicated the presence of mesopores in C-Fe-UFR (Fig. 2(c)). C-Fe-UFR showed a BET surface area of 433.56 $cm^2 \cdot g^{-1}$ and a total pore volume of 1.14 $cm^3 \cdot g^{-1}$, which are higher than the values of C-UFR/Fe (284.65 $cm^2 \cdot g^{-1}$ and 0.50 $cm^3 \cdot g^{-1}$, respectively) and slightly lower than those of C-UFR (449.83 $cm^2 \cdot g^{-1}$ and 1.90 $cm^3 \cdot g^{-1}$, respectively) (Fig. S8 in the ESM). Interestingly, C-Fe-UFR possesses a hierarchical mesoporous structure, which provides abundant active sites and highly efficient mass diffusion channels for the ORR. The XRD pattern of C-Fe-UFR displays two broad peaks at ~25° and 44° (Fig. S9 in the ESM), representing the (002) plane of the graphite structure and the (101) plane of disordered amorphous carbon, respectively. The corresponding Raman spectrum shows an increased D/G peak intensity ratio for C-Fe-UFR compared to those of C-UFR and C-UFR/Fe (Fig. S10 in the ESM), which indicates an increased fraction of the amorphous and defect carbon structures.

Energy-dispersive X-ray spectroscopy (EDS) was used to confirm the elemental composition of C-Fe-UFR (Table S1 in the ESM), and the corresponding elemental mapping in Fig. 2(d) illustrates the homogeneous distribution of carbon, nitrogen, and iron over the C-Fe-UFR skeleton. The N content of C-Fe-UFR was determined as 4.47%, exceeding that of its counterparts (2.04% for C-UFR and 4.17% for C-UFR/Fe). The Fe content was determined as 0.45% for C-Fe-UFR and 0.21% for C-UFR/Fe. The higher content of Fe in C-Fe-UFR compared to C-UFR/Fe is the result of coordination of Fe ions by multiple donor amino groups in Fe-UFR. In contrast, the introduction of iron into Fe-UFR and UFR/Fe also increases the post-heating N content compared to UFR. The chemical composition and effect of N doping were subsequently investigated by XPS. The N 1s XPS peaks of C-Fe-UFR were deconvoluted into four peaks corresponding to pyridinic N (398.8 eV), pyrrolic N (400.3 eV), quaternary N (401.2 eV), and pyridinic N-oxidized (402.5 eV) species (Fig. S11 in the ESM) [43]. The corresponding nitrogen species were also dominant in the case of C-UFR/Fe and C-UFR catalysts. The positive binding

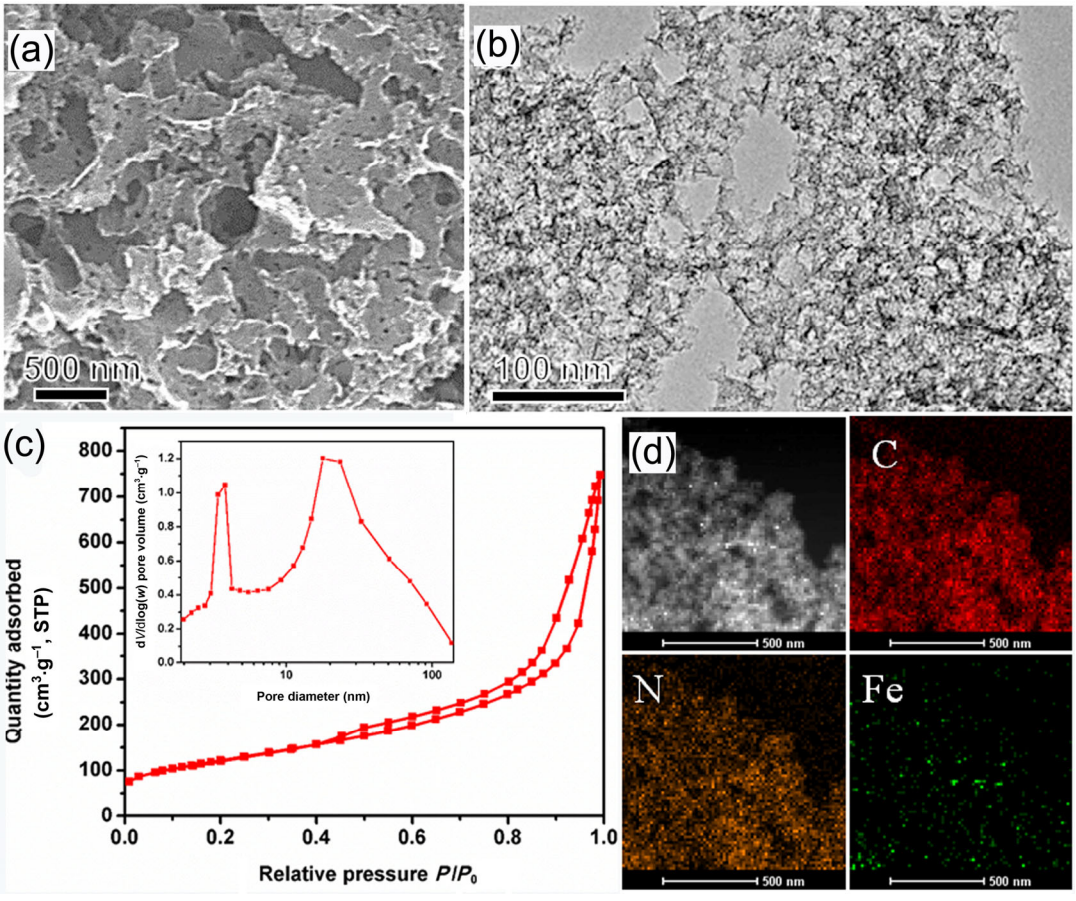

Figure 2 (a) SEM and (b) TEM images of C-Fe-UFR. (c) Nitrogen adsorption–desorption isotherm of C-Fe-UFR (inset: pore size distribution of C-Fe-UFR). (d) High-angle annular dark-field scanning transmission electron microscopy (HAADF-STEM) image and the corresponding carbon, nitrogen, and iron elemental mapping images.

energy shift for pyridinic and pyrrolic N species compared to C-UFR might arise from their coordination with Fe [44, 45], with the higher content of pyridinic and pyrrolic N compared to C-UFR/Fe benefiting the intrinsic homogeneous Fe chelation in UFR. The Fe 2p spectrum of C-Fe-UFR (Fig. S12 in the ESM) shows peaks at 706.9 eV (metallic Fe), 709.4 eV (Fe coordinated by N), and two peaks at 711.4 and 713.3 eV accompanied by satellite peaks at binding energies higher than 714 eV, which were ascribed to different oxides [46]. Thus, it was shown that metal species stabilized by nitrogen coordination are responsible for producing catalysts with ORR activity [44–46].

The ORR catalytic activities of as-prepared samples were investigated in 0.1 M KOH. No redox peak was observed in the cyclic voltammograms (CVs) of C-Fe-UFR in N_2-saturated solution. In sharp contrast, a well-defined cathodic peak appeared at ~0.85 V (Fig. S13 in the ESM) when the solution was saturated with O_2, confirming the ORR electrocatalytic activity [47]. RDE measurements in O_2-saturated electrolytes show that the optimal ORR performance (Fig. S14 in the ESM) is achieved for a temperature of 900 ˚C and a Fe content of 1.21 (1.21 g ferric nitrate: 1.8 g urea) in Fe-UFR, probably corresponding to an optimal balance of surface area, active site density, and the high graphitization degree required for good electron conductivity. According to the RDE polarization curves, C-Fe-UFR exhibits a more positive onset potential (1.01 V) with a half-wave potential of 0.86 V and a higher limiting current density (5.72 mA·cm^{-2}) than Pt/C, indicating better performance. To gain insight into the origin of such high activity, we performed comparative measurements for C-UFR/Fe and C-UFR. C-UFR/Fe exhibited a much lower cathodic current density and a more negative half-wave potential due

to its lower BET surface area, pore volume, and Fe-N content originating from the agglomeration of metal particles and microstructural inhomogeneity. Despite the higher surface area and graphitization degree required for good electron conductivity, both C-Fe-UFR and C-UFR/Fe are more active than C-UFR, as proven by their more positive onset and half-wave potentials (Fig. 3(a)), supporting the notion that transition metals are needed to produce highly active catalysts [45]. To the best of our knowledge, the ORR activity exhibited by C-Fe-UFR is among the highest reported for N-doped carbon-based non-precious metal carbons (NPMCs) (Table S2 in the ESM).

RRDE measurements were performed to detect the formation of peroxide (HO_2^-) and quantify the ORR pathway for C-Fe-UFR. The yields and electron transfer numbers (n) of HO_2^- are illustrated in Fig. 3(b). The HO_2^- yield in the potential range from 0.2 to 0.8 V was less than 6%, while the n value of 3.93–3.98 was close to that of Pt/C, confirming a nearly four-electron pathway for C-Fe-UFR. In contrast, the C-UFR/Fe and C-UFR catalysts showed higher HO_2^- yields and smaller electron transfer numbers, indicating a higher contribution of two-electron pathways.

Catalyst durability is crucial for practical applications, and hence, the durability of the C-Fe-UFR catalyst was evaluated in an accelerated manner. As displayed in Fig. 3(c), C-Fe-UFR exhibits excellent long-term stability with a much smaller half-wave potential negative shift (22 mV) after 10,000 cycles compared to that of Pt/C (33 mV). Subsequently, CVs were recorded to test the possible methanol crossover effect. The almost unchanged ORR peak current for C-Fe-UFR (in contrast to Pt/C) shown in Fig. 3(d) suggests its high ORR electrocatalytic selectivity with a strong tolerance to the methanol crossover effect.

More importantly, the C-Fe-UFR catalyst also exhibits a competitive electrocatalytic ORR performance in acidic medium (0.1 M $HClO_4$), as proven by the ORR polarization curves in Fig. S15(a) in the ESM, showing an onset potential of 0.872 V that is close to that of Pt/C (0.990 V). The half-wave potential of C-Fe-UFR is 0.73 V, only ~57 mV lower than that of Pt/C. Although C-Fe-UFR is less active in acidic media compared to

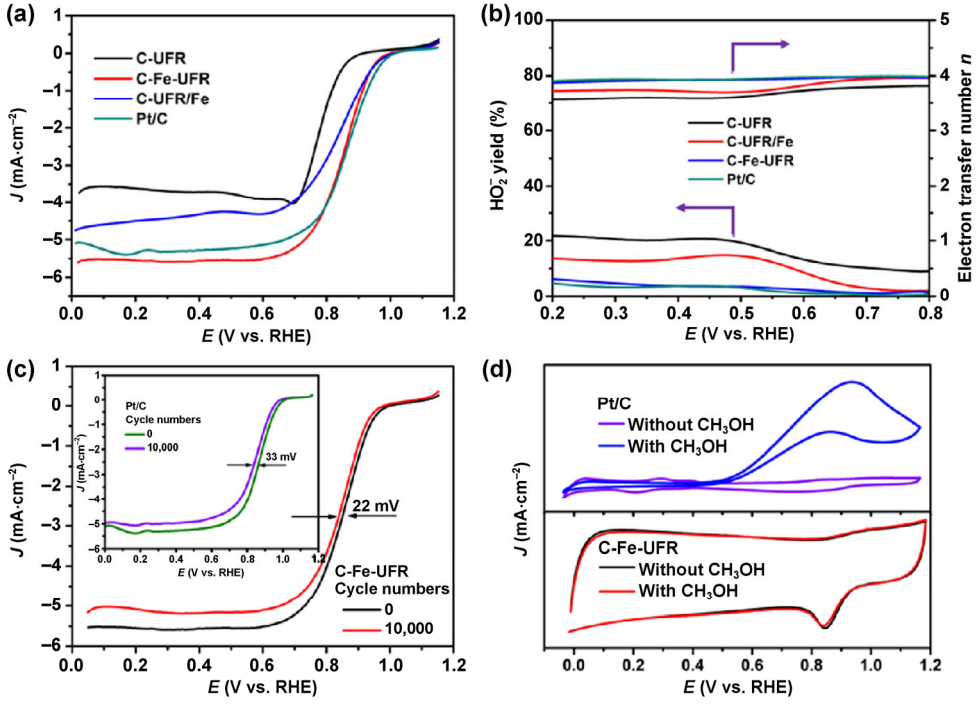

Figure 3 (a) RDE polarization curves for C-Fe-UFR, C-UFR/Fe, C-UFR, and Pt/C in O_2-saturated 0.1 M KOH recorded at a scan rate of 10 mV·s^{-1} and a rotation speed of 1,600 rpm. (b) HO_2^- yields and electron transfer numbers of C-Fe-UFR, C-UFR/Fe, C-UFR, and Pt/C at various potentials based on the corresponding RRDE data. (c) ORR polarization curves of C-Fe-UFR before and after 10,000 potential cycles in O_2-saturated electrolyte (inset shows the corresponding curves for Pt/C). (d) CVs of C-Fe-UFR and Pt/C in O_2-saturated and 3 M methanol/O_2-saturated 0.1 M KOH recorded at a scan rate of 50 mV·s^{-1}.

alkaline conditions, it is still one of the best carbon-based NPMCs recently reported for similar conditions (Table S3 in the ESM). The C-Fe-UFR catalyst also shows an ORR stability similar to that of Pt/C, as revealed by its slight negative half-wave potential shift, which is only ~5 mV lower than that of Pt/C (Figs. S15(b) and S15(c) in the ESM). C-Fe-UFR also exhibits high ORR selectivity with a strong tolerance to the methanol crossover effect (Fig. S15(f) in the ESM).

The oxygen evolution activity of C-Fe-UFR was estimated and compared with C-UFR/Fe, C-UFR, and Pt/C. As shown in Fig. 4(a), the operating potential required for the C-Fe-UFR catalyst to deliver a current density of 10 mA·cm^{-2} is 1.68 V, which compares favorably to other reported carbon-based catalysts (Table S4 in the ESM). Additionally, RDE measurements (Fig. S16 in the ESM) show that the best performance is achieved for a Fe content of 1.21. In contrast, C-UFR/Fe and C-UFR achieve a current density of 10 mA·cm^{-2} at potentials of 1.76 and 1.80 V respectively, which are much higher than that of C-Fe-UFR, implying the superior OER activity of C-Fe-UFR due to its higher nitrogen content, higher surface area, and a special hierarchical mesoporous structure. For the Pt/C catalyst, a potential of ~1.91 V is required to realize a current density of 10 mA·cm^{-2}, approximately ~220 mV higher than that of C-Fe-UFR. The kinetics of the catalytic OER was further examined using Tafel plots. The Tafel slope for C-Fe-UFR is about 160 mV·decade^{-1}, much smaller than those of C-UFR/Fe (178 mV·decade^{-1}), C-UFR (213 mV·decade^{-1}), and Pt/C catalysts (287 mV·decade^{-1}), which further confirms its superior electrochemical OER performance (Fig. 4(b)).

To assess the OER stability of C-Fe-UFR, a chronoamperometric test was carried out. C-Fe-UFR exhibited a slow decrease in current with 80% retention over 10,000 s of continuous operation, whereas Pt/C experienced a faster current loss with only 48% retention (Fig. S17 in the ESM).

Encouraged by the high ORR and OER electrocatalytic activity of C-Fe-UFR, Zn–air batteries (Fig. 5(a)), which have been widely proposed as a promising electrical energy storage system, were fabricated using the C-Fe-UFR catalyst as a cathode, achieving an open circuit voltage of ~1.40 V. The corresponding polarization curves and power density plots reveal the superior performance of Zn–air batteries based on C-Fe-UFR, which reach a peak power density of 142 mW·cm^{-2} at 0.65 V, as compared to the Pt/C-based batteries that show a value of 102 mW·cm^{-2} (Fig. 5(b)).

Discharge plateaus at about 1.16 and 1.12 V could be observed in the galvanostatic discharge curves of C-Fe-UFR and Pt/C at a current rate of 50 mA·cm^{-2} (Fig. 5(c)), with only a slight voltage drop observed for long-term discharge. The observed specific capacities of C-Fe-UFR based Zn–air battery normalized to the mass of consumed Zn equaled 467 and 438 mAh·g^{-1} at current rates of 10 and 50 mA·cm^{-2} (Fig. 5(d)). Figure 5(e) shows the charge and discharge polarization curves of a rechargeable Zn–air battery, the difference value between charge and discharge potentials of C-Fe-UFR is 1.31 V at a current density of 50 mA·cm^{-2} lower than that of Pt/C (1.92 V). The C-Fe-UFR catalyst showed a high round-trip efficiency during long-term charge–discharge cycling tests at a constant current density of 10 mA·cm^{-2}, with a negligible voltage change after

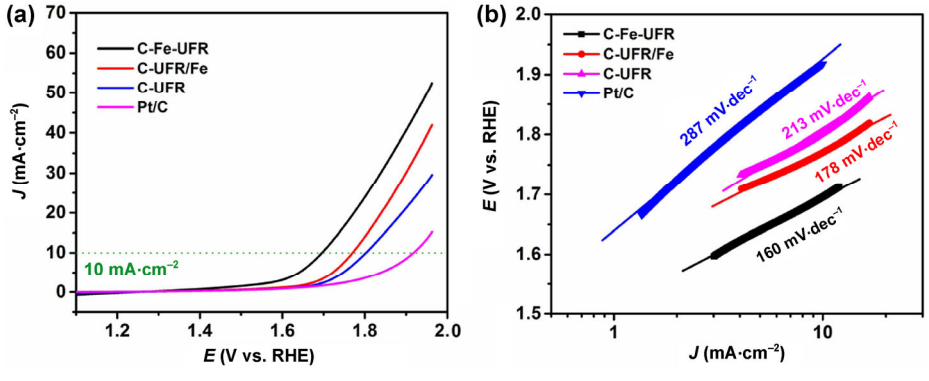

Figure 4 (a) OER polarization curves for C-Fe-UFR, C-UFR/Fe, C-UFR, and Pt/C in 0.1 M KOH recorded at a scan rate of 10 mV·s^{-1} and a rotation speed of 1,600 rpm. (b) Tafel plots for C-Fe-UFR, C-UFR/Fe, C-UFR, and Pt/C.

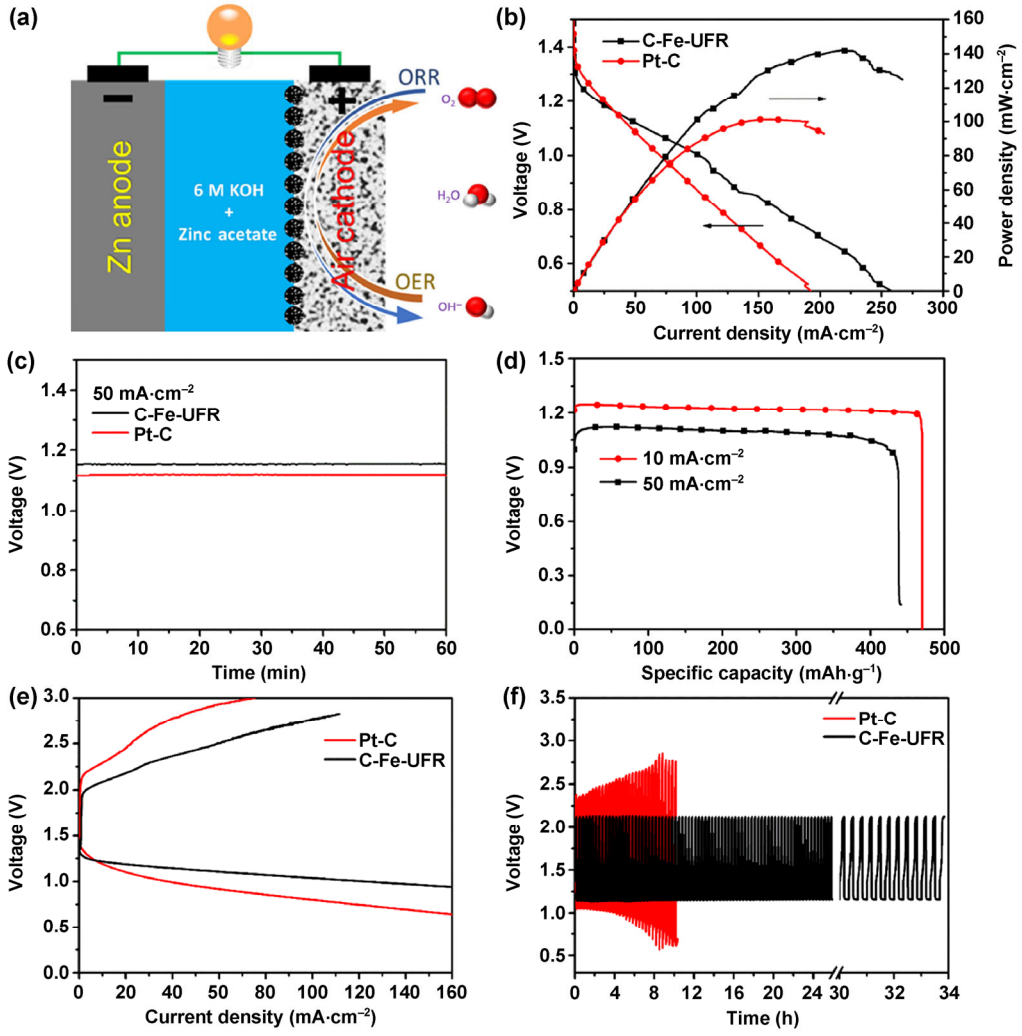

Figure 5 (a) Scheme of the Zn–air battery. (b) The voltages and power densities of Zn–air batteries with C-Fe-UFR and Pt/C cathodes. (c) Typical galvanostatic discharge curves of Zn–air batteries based on C-Fe-UFR and Pt/C at a current density of 50 mA·cm^{-2}. (d) Typical continuous discharge curves of Zn–air batteries based on a C-Fe-UFR cathode carried out at two different current densities until complete consumption of Zn. The specific capacity was normalized to the mass of consumed Zn. (e) Charge and discharge polarization curves of a rechargeable Zn–air battery. (f) Discharge–charge curves of Zn–air batteries at a current density of 10 mA·cm^{-2} (20 min per cycle) for C-Fe-UFR and Pt/C.

100 cycles (about 34 h), in sharp contrast to the greatly increased overpotential for Pt/C after ~10 h (Fig. 5(f)).

4 Conclusions

In summary, as a proof-of-concept experiment, we developed and demonstrated a novel instantaneous (20 s) one-step scalable synthesis of a novel Fe-UFR hydrogel, which intrinsically ensures atomic-level dispersion of Fe ions in UFR. When used as an all-in-one precursor for the synthesis of porous Fe-N-C electrocatalysts, the atomic-level dispersion prevents the agglomeration of metal particles and guarantees the microstructural homogeneity of the C-Fe-UFR produced during pyrolysis. The C-Fe-UFR electrocatalyst exhibits high catalytic activity and durability for both ORR and OER (compared to Pt/C), rendering it a high-performance cheap bifunctional electrocatalyst. Furthermore, much better performances including higher power density and better cycling stability were obtained for rechargeable Zn–air batteries based on the above catalyst. The strategy demonstrated

herein may initiate the sustainable development of other hydrogel-derived carbon-based catalysts for different electrochemical energy conversion and storage systems.

Acknowledgements

This work is financially supported by the National Basic Research Program of China (No. 2012CB215500), Foundation for Innovative Research Groups of the National Natural Science Foundation of China (No. 20921002), National Natural Science Foundation of China (No. 21101147).

Electronic Supplementary Material: Supplementary material (photographs, TEM imaging, Raman spectroscopy measurements, XRD patterns, XPS characterization, electrochemical measurements, etc.) is available in the online version of this article at http://dx.doi.org/10.1007/s12274-016-1343-z.

References

[1] Ma, T. Y.; Dai, S.; Jaroniec, M.; Qiao, S. Z. Metal–organic framework derived hybrid Co_3O_4-carbon porous nanowire arrays as reversible oxygen evolution electrodes. *J. Am. Chem. Soc.* **2014**, *136*, 13925–13931.

[2] Liang, Y. Y.; Li, Y. G.; Wang, H. L.; Zhou, J. G.; Wang, J.; Regier, T.; Dai, H. J. Co_3O_4 nanocrystals on graphene as a synergistic catalyst for oxygen reduction reaction. *Nat. Mater.* **2011**, *10*, 780–786.

[3] Wang, J.; Li, K.; Zhong, H. X.; Xu, D.; Wang, Z. L.; Jiang, Z.; Wu, Z. J.; Zhang, X. B. Synergistic effect between metal-nitrogen-carbon sheets and NiO nanoparticles for enhanced electrochemical water-oxidation performance. *Angew. Chem., Int. Ed.* **2015**, *54*, 10530–10534.

[4] Li, Y. G.; Zhou, W.; Wang, H. L.; Xie, L. M.; Liang, Y. Y.; Wei, F.; Idrobo, J. C.; Pennycook, S. J.; Dai, H. J. An oxygen reduction electrocatalyst based on carbon nanotube-graphene complexes. *Nat. Nanotechnol.* **2012**, *7*, 394–400.

[5] Li, Y. G.; Dai, H. J. Recent advances in zinc–air batteries. *Chem. Soc. Rev.* **2014**, *43*, 5257–5275.

[6] Zhang, T.; Zhou, H. S. A reversible long-life lithium-air battery in ambient air. *Nat. Commun.* **2013**, *4*, 1817.

[7] He, W. H.; Jiang, C. H.; Wang, J. B.; Lu, L. H. High-rate oxygen electroreduction over graphitic-N species exposed on 3D hierarchically porous nitrogen-doped carbons. *Angew. Chem., Int. Ed.* **2014**, *53*, 9503–9507.

[8] Cheon, J. Y.; Kim, J. H.; Kim, J. H.; Goddeti, K. C.; Park, J. Y.; Joo, S. H. Intrinsic relationship between enhanced oxygen reduction reaction activity and nanoscale work function of doped carbons. *J. Am. Chem. Soc.* **2014**, *136*, 8875–8878.

[9] Liu, Y. W.; Cheng, H.; Lyu, M. J.; Fan, S. J.; Liu, Q. H.; Zhang, W. S.; Zhi, Y. D.; Wang, C. M.; Xiao, C.; Wei, S. Q. et al. Low overpotential in vacancy-rich ultrathin $CoSe_2$ nanosheets for water oxidation. *J. Am. Chem. Soc.* **2014**, *136*, 15670–15675.

[10] Fominykh, K.; Feckl, J. M.; Sicklinger, J.; Döblinger, M.; Böcklein, S.; Ziegler, J.; Peter, L.; Rathousky, J.; Scheidt, E. W.; Bein, T. et al. Ultrasmall dispersible crystalline nickel oxide nanoparticles as high-performance catalysts for electrochemical water splitting. *Adv. Funct. Mater.* **2014**, *24*, 3123–3129.

[11] Kramm, U. I.; Lefevre, M.; Larouche, N.; Schmeisser, D.; Dodelet, J. P. Correlations between mass activity and physicochemical properties of Fe/N/C catalysts for the ORR in PEM fuel cell via ^{57}Fe Mössbauer spectroscopy and other techniques. *J. Am. Chem. Soc.* **2014**, *136*, 978–985.

[12] Chang, S. T.; Wang, C. H.; Du, H. Y.; Hsu, H. C.; Kang, C. M.; Chen, C. C.; Wu, J. C. S.; Yen, S. C.; Huang, W. F.; Chen, L. C. et al. Vitalizing fuel cells with vitamins: Pyrolyzed vitamin B12 as a non-precious catalyst for enhanced oxygen reduction reaction of polymer electrolyte fuel cells. *Energy Environ. Sci.* **2012**, *5*, 5305–5314.

[13] Deng, D. H.; Yu, L.; Chen, X. Q.; Wang, G. X.; Jin, L.; Pan, X. L.; Deng, J.; Sun, G. Q.; Bao, X. H. Iron encapsulated within pod-like carbon nanotubes for oxygen reduction reaction. *Angew. Chem., Int. Ed.* **2013**, *52*, 371–375.

[14] Trotochaud, L.; Young, S. L.; Ranney, J. K.; Boettcher, S. W. Nickel–iron oxyhydroxide oxygen-evolution electrocatalysts: The role of intentional and incidental iron incorporation. *J. Am. Chem. Soc.* **2014**, *136*, 6744–6753.

[15] Takeguchi, T.; Yamanaka, T.; Takahashi, H.; Watanabe, H.; Kuroki, T.; Nakanishi, H.; Orikasa, Y.; Uchimoto, Y.; Takano, H.; Ohguri, N. et al. Layered perovskite oxide: A reversible air electrode for oxygen evolution/reduction in rechargeable metal-air batteries. *J. Am. Chem. Soc.* **2013**, *135*, 11125–11130.

[16] Suntivich, J.; May, K. J.; Gasteiger, H. A.; Goodenough, J. B.; Shao-Horn, Y. A perovskite oxide optimized for oxygen evolution catalysis from molecular orbital principles. *Science* **2011**, *334*, 1383–1385.

[17] Li, Q.; Cao, R. G.; Cho, J.; Wu, G. Nanocarbon electrocatalysts for oxygen reduction in alkaline media for advanced energy conversion and storage. *Adv. Energy Mater.* **2014**, *4*, 1301415.

[18] Liu, Q.; Wang, Y. B.; Dai, L. M.; Yao, J. N. Scalable fabrication of nanoporous carbon fiber films as bifunctional catalytic electrodes for flexible Zn-air batteries. *Adv. Mater.* **2016**, *28*, 3000–3006.

[19] Gorlin, Y.; Jaramillo, T. F. A bifunctional nonprecious metal catalyst for oxygen reduction and water oxidation. *J. Am. Chem. Soc.* **2010**, *132*, 13612–13614.

[20] Li, G.; Wang, X. L.; Fu, J.; Li, J. D.; Park, M. G.; Zhang, Y. N.; Lui, G.; Chen, Z. W. Pomegranate-inspired design of highly active and durable bifunctional electrocatalysts for rechargeable metal–air batteries. *Angew. Chem., Int. Ed.* **2016**, *55*, 4977–4982.

[21] Liu, Q.; Jin, J. T.; Zhang, J. Y. $NiCo_2S_4$@graphene as a bifunctional electrocatalyst for oxygen reduction and evolution reactions. *ACS Appl. Mater. Interfaces* **2013**, *5*, 5002–5008.

[22] Liang, Y. Y.; Li, Y. G.; Wang, H. L.; Dai, H. J. Strongly coupled inorganic/nanocarbon hybrid materials for advanced electrocatalysis. *J. Am. Chem. Soc.* **2013**, *135*, 2013–2036.

[23] Wang, S. Y.; Zhang, L. P.; Xia, Z. H.; Roy, A.; Chang, D. W.; Baek, J. B.; Dai, L. M. BCN graphene as efficient metal-free electrocatalyst for the oxygen reduction reaction. *Angew. Chem., Int. Ed.* **2012**, *51*, 4209–4212.

[24] Tian, G. L.; Zhao, M. Q.; Yu, D. S.; Kong, X. Y.; Huang, J. Q.; Zhang, Q.; Wei, F. Nitrogen-doped graphene/carbon nanotube hybrids: *In situ* formation on bifunctional catalysts and their superior electrocatalytic activity for oxygen evolution/reduction reaction. *Small* **2014**, *10*, 2251–2259.

[25] Zhao, Y.; Nakamura, R.; Kamiya, K.; Nakanishi, S.; Hashimoto, K. Nitrogen-doped carbon nanomaterials as non-metal electrocatalysts for water oxidation. *Nat. Commun.* **2013**, *4*, 2390.

[26] Walcarius, A. Mesoporous materials and electrochemistry. *Chem. Soc. Rev.* **2013**, *42*, 4098–4140.

[27] Silva, R.; Voiry, D.; Chhowalla, M.; Asefa, T. Efficient metal-free electrocatalysts for oxygen reduction: Polyaniline-derived N- and O-doped mesoporous carbons. *J. Am. Chem. Soc.* **2013**, *135*, 7823–7826.

[28] Sevilla, M.; Valle-Vigón, P.; Fuertes, A. B. N-doped polypyrrole-based porous carbons for CO_2 capture. *Adv. Funct. Mater.* **2011**, *21*, 2781–2787.

[29] Roberts, A. D.; Li, X.; Zhang, H. F. Porous carbon spheres and monoliths: Morphology control, pore size tuning and their applications as Li-ion battery anode materials. *Chem. Soc. Rev.* **2014**, *43*, 4341–4356.

[30] Tian, J.; Morozan, A.; Sougrati, M. T.; Lefèvre, M.; Chenitz, R.; Dodelet, J. P.; Jones, D.; Jaouen, F. Optimized synthesis of Fe/N/C cathode catalysts for PEM fuel cells: A matter of iron-ligand coordination strength. *Angew. Chem., Int. Ed.* **2013**, *52*, 6867–6870.

[31] Zhao, D.; Shui, J. L.; Chen, C.; Chen, X. Q.; Reprogle, B. M.; Wang, D. P.; Liu, D. J. Iron imidazolate framework as precursor for electrocatalysts in polymer electrolyte membrane fuel cells. *Chem. Sci.* **2012**, *3*, 3200–3205.

[32] Zhao, Y.; Watanabe, K.; Hashimoto, K. Efficient oxygen reduction by a Fe/Co/C/N nano-porous catalyst in neutral media. *J. Mater. Chem. A* **2013**, *1*, 1450–1456.

[33] Wu, G.; More, K. L.; Johnston, C. M.; Zelenay, P. High-performance electrocatalysts for oxygen reduction derived from polyaniline, iron, and cobalt. *Science* **2011**, *332*, 443–447.

[34] Zhao, Y.; Kamiya, K.; Hashimoto, K.; Nakanishi, S. Efficient bifunctional Fe/C/N electrocatalysts for oxygen reduction and evolution reaction. *J. Phys. Chem. C* **2015**, *119*, 2583–2588.

[35] Chen, X. Y.; Chen, C.; Zhang, Z. J.; Xie, D. H.; Deng, X.; Liu, J. W. Nitrogen-doped porous carbon for supercapacitor with long-term electrochemical stability. *J. Power Sources* **2013**, *230*, 50–58.

[36] Liu, Z.; Du, Z. Y.; Song, H.; Wang, C. Y.; Subhan, F.; Xing, W.; Yan, Z. F. The fabrication of porous N-doped carbon from widely available urea formaldehyde resin for carbon dioxide adsorption. *J. Colloid Interface Sci.* **2014**, *416*, 124–132.

[37] Su, D. S.; Sun, G. Q. Nonprecious-metal catalysts for low-cost fuel cells. *Angew. Chem., Int. Ed.* **2011**, *50*, 11570–11572.

[38] Xiang, Z. H.; Xue, Y. H.; Cao, D. P.; Huang, L.; Chen, J. F.; Dai, L. M. Highly efficient electrocatalysts for oxygen reduction based on 2D covalent organic polymers complexed with non-precious metals. *Angew. Chem., Int. Ed.* **2014**, *53*, 2433–2437.

[39] Cao, R. G.; Lee, J. S.; Liu, M. L.; Cho, J. Recent progress in non-precious catalysts for metal-air batteries. *Adv. Energy Mater.* **2012**, *2*, 816–829.

[40] Nishat, N.; Ahmad, S.; Ahamad, R. T. Synthesis and characterization of antibacterial polychelates of urea–formaldehyde resin with Cr(III), Mn(II), Fe(III), Co(II), Ni(II), Cu(II), and Zn(II) metal ions. *J. Appl. Polym. Sci.* **2006**, *100*, 928–936.

[41] Wei, Z. J.; He, J.; Liang, T.; Oh, H.; Athas, J.; Tong, Z.; Wang, C. Y.; Nie, Z. H. Autonomous self-healing of poly(acrylic acid) hydrogels induced by the migration of ferric ions. *Polym. Chem.* **2013**, *4*, 4601–4605.

[42] Pratt, T. J.; Johns, W. E.; Rammon, R. M.; Plagemann, W. L. A novel concept on the structure of cured urea-formaldehyde resin. *J. Adhesion* **1985**, *17*, 275–295.

[43] Liu, J.; Sun, X. J.; Song, P.; Zhang, Y. W.; Xing, W.; Xu, W. L. High-performance oxygen reduction electrocatalysts

based on cheap carbon black, nitrogen, and trace iron. *Adv. Mater.* **2013**, *25*, 6879–6883.

[44] Liang, J.; Zhou, R. F.; Chen, X. M.; Tang, Y. H.; Qiao, S. Z. Fe–N decorated hybrids of CNTs grown on hierarchically porous carbon for high-performance oxygen reduction. *Adv. Mater.* **2014**, *26*, 6074–6079.

[45] Wu, J.; Li, W. M.; Higgins, D.; Chen, Z. W. Heat-treated nonprecious catalyst using Fe and nitrogen-rich 2,3,7,8-tetra(pyridin-2-yl)pyrazino[2,3-*g*]quinoxaline coordinated complex for oxygen reduction reaction in PEM fuel cells. *J. Phys. Chem. C* **2011**, *115*, 18856–18862.

[46] Wang, L.; Yin, J.; Zhao, L.; Tian, C. G.; Yu, P.; Wang, J. Q.; Fu, H. G. Ion-exchanged route synthesis of Fe_2N-N-doped graphitic nanocarbons composite as advanced oxygen reduction electrocatalyst. *Chem. Commun.* **2013**, *49*, 3022–3024.

[47] Yang, D. S.; Bhattacharjya, D.; Inamdar, S.; Park, J.; Yu, J. S. Phosphorus-doped ordered mesoporous carbons with different lengths as efficient metal-free electrocatalysts for oxygen reduction reaction in alkaline media. *J. Am. Chem. Soc.* **2012**, *134*, 16127–16130.